




Probing into photoluminescence properties of trivalent rare earths ($\text{Gd}^{3+}/\text{Tb}^{3+}/\text{Dy}^{3+}/\text{Eu}^{3+}$) activated fluoro-elpasolites

Vartika S. Singh^{1,*} , S. R. Dhakate^{1,*}, P. V. Tumram², P. D. Belsare³, and S. V. Moharil⁴

¹Advanced Carbon Products and Metrology, CSIR-NPL, Dr. K. S. Krishnan Marg, New Delhi 110012, India

²Department of Physics, Amolakchand Mahavidyalaya, Yavatmal, Maharashtra 445001, India

³Shri Ramdeobaba College of Engineering and Management, Katol Road, Nagpur 440013, India

⁴University Department of Physics, R. T. M. Nagpur University, Nagpur 440033, India

Received: 28 November 2022

Accepted: 21 April 2023

Published online:

4 May 2023

© The Author(s), under exclusive licence to Springer Science+Business Media, LLC, part of Springer Nature 2023

ABSTRACT

Natural K_2NaAlF_6 compound is known to exist in elpasolite structure form, since years. In recent times, such fluoro-elpasolites activated by small amounts of Mn^{4+} have emerged as most propitious red-phosphor for solid-state lighting purposes. Fluoro-elpasolites such as K_2LiAlF_6 and K_2NaAlF_6 are easy to prepare via simple precipitation method. In present work, fresh photoluminescence studies on rare earth-doped trivalent ions are reported in these hosts. Gadolinium added phosphors showed interesting PL properties with different concentrations. Also, really long lifetimes of luminescence decay curves were recorded for these phosphors. Other dopants such as terbium, dysprosium and europium in their trivalent form also showed their characteristic PL spectra. Previously, PL studies on Eu^{2+} and Ce^{3+} doped on these compounds have been already done and reported elsewhere. Phase-structural, morphological and elemental analysis has been also carried out on these compounds using various XRD, SEM and EDS techniques. Particles are found to be of bigger size than $1\ \mu\text{m}$ i.e. in micro-range using DLS measurement. In the end, CIE coordinates and CCT(K) were calculated for phosphors, with PL emissions lying within the visible range of radiation spectrum.

1 Introduction

Elpasolites as the name suggests, K_2NaAlF_6 is the mineral found and named after its discovery from El Paso County, Colorado, United States in 1883 [1].

Addition of LiF to elpasolite structure, led to formation of K_2LiAlF_6 phase [2, 3]. Initial structural studies related to these phases go back to 1971 when Grjotheim et al. [4] found an intermediate phase- K_2LiAlF_6 (melts incongruently at $780\ ^\circ\text{C}$) while investigating a

Address correspondence to E-mail: vartikasinh1710@gmail.com; dhakate@nplindia.org

binary alkali cryolites Li_3AlF_6 - K_3AlF_6 system. Later, another compound K_2NaAlF_6 was uncovered in the system K_3AlF_6 - Na_3AlF_6 which melts congruently at 954 °C [5]. Earlier, Bukhalova and Mal'tsev [6–8] and Edoyan et al. [9] have also worked on corresponding systems prior to 1970's but Sorrell and Groetsch in 1986 [10] probed deeper into and mentioned a compositional range for K_2NaAlF_6 from 60/40 to 25/75% in ratios of Na_3AlF_6 / K_3AlF_6 . One of the preliminary studies related to luminescence on these hexafluoroaluminates comprises of trivalent chromium activated K_2NaAlF_6 [11] and K_2LiAlF_6 [12], while a technological breakthrough was achieved when KL/NAF found its chief application in new white light-emitting diodes.

Fluoro-elpasolites with formula A_2BMF_6 (where, 'A & B' represent alkali metals, 'M' as transition metals) are considered as double perovskites [13, 14] which are believed to follow a general relation, known as Goldschmidt's tolerance factor 't', described as:

$$t = \frac{\sqrt{2}(r_A + r_F)}{r_B + r_M + 2r_F}$$

where, r_A , r_B , r_M and r_F are the ionic radii of the corresponding ions in the general formula. A cubic phase is stable for fluorides in the region of $0.85 < t < 1$. For larger t values ($t > 1$), the elpasolite phase exhibits hexagonal or rhombohedral symmetry with complete rearrangement of the structure [15].

Compared to their other counterparts like chlorides, bromides, iodides etc., fluorides are much less hygroscopic and acquire high optical standards. Despite of possessing high quality aspects, fluorides are not convenient to study due to complicated syntheses techniques. Ages old syntheses procedures involve huge and bulky apparatus, high temperatures, flowing of HF-gas through furnaces etc. [4, 5, 10] which involve high risk of accidents. Therefore, we established a simple one-step route through wet-chemical synthesis for phase-pure preparation of fluorides.

We investigated and reported some photoluminescence observations on Eu^{2+} & Ce^{3+} -activated KL/NAF in 2014 [16] and 2015 [17] and found enormous potential of these compounds as exceptionally efficient phosphors which encouraged us to work further and investigate these systems.

In recent years, many reports featuring red luminescence due to Mn^{4+} in KL/NAF have appeared.

These compositions have been explored in great details [18–28]. White light-emitting diodes (w-LEDs) dominate the field of solid-state lighting due to their high efficiency and longer lifetimes over normal incandescent and fluorescent lamps. But conventional w-LEDs consisting of a yellow phosphor $\text{Y}_3\text{Al}_5\text{O}_{12}:\text{Ce}^{3+}$ (YAG: Ce^{3+}) coated on a blue-emitting InGaN chip suffer from a drawback of red-colour component deficiency. Therefore, to increase the CRI value of the tri-colours lamp, use of new red-emitting phosphors became important. However, initial research was more focussed on Mn^{4+} -doped binary-alkaline fluoride phosphors ($\text{A}_2\text{XF}_6:\text{Mn}^{4+}$ (as A = K, Na, Cs and X = Si, Ge or Ti)), as red emitting components [18]. Later, ternary-alkaline fluoroaluminates such as KLAf & KNAf demonstrated better photoluminescence (PL) efficacy on LEDs (with emissions in the 600–650 nm range). Transition metal Mn^{4+} activated phosphors absorb in blue region and show intense emission in red due to unique $3d^3$ electronic configuration of Mn^{4+} .

Although use of HF in synthesis procedures is hazardous, doping of Manganese in its tetra-valent state is rather a difficult task. Synthesis of Mn^{4+} -activated fluoride phosphors is a two step process and requires synthesis of K_2MnF_6 prior to formation of the actual compound. While we observed that synthesis through direct use of HF as precipitating agent is rather a much simpler process.

Also, it can be suggested from the previous research works that K_2LiAlF_6 always precipitates in hexagonal form during precipitation method [20], whereas its cubic phase forms in hydrothermal process [19].

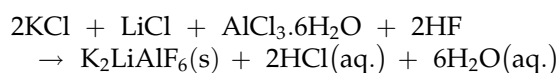
2 Experimental

Fluoro-elpasolites KLAf & KNAf have been prepared by simple wet-chemical synthesis method as described in our previous publications [16, 17]. Aqueous solutions of KCl, LiCl and $\text{AlCl}_3 \cdot 6\text{H}_2\text{O}$ have been prepared separately (in stoichiometric ratios) by dissolving in D.I. water. All the solutions were mixed together and transferred to a PTFE beaker. A precipitate forms on drop wise addition of HF (48%) at more than 85 °C. This precipitate was considered for further characterizations after filtration process.

Repeated synthesis procedure reveals, high yield in precipitation at boiling temperatures. pH value was

found to be around 3.4 for K_2LiAlF_6 , whereas it varies between 0.40 and 3 for different dopants in K_2NaAlF_6 . Various rare earth ions such as gadolinium/europium/terbium/dysprosium were added as activators. Initially, oxides of these RE^{3+} activators were taken. Aq. chloride solutions were prepared by dissolving these oxides in minimal amount of [HCl + D.I.water] and then, mixing them to the rest of the alkali-chloride solution prior to addition of HF. pH value of the entire solution highly depends upon the amount of Cl^- ions present in the solution.

Chemical reaction could be expressed in the following way (for compound formation only):



Here, K_2LiAlF_6 precipitates in solid form and could be separated using simple filtration techniques. The collected powder on the filter paper can be either dried by blowing air, or by keeping in the oven nearly at 60 °C overnight. Considering ' K^+ ' as the host substitutional site for the respective RE^{3+} impurity ion in KLAf, the formula for x mol% conc. of RE^{3+} ion can be written as $K_{2(1-x)}RE^{3+}_{2x}LiAlF_{6+4x}$. Typically, for adding 5 mol% Gd^{3+} ions to the KLAf crystal structure we used, $KCl = 1.1734$ gm, $LiCl = 0.3512$ gm, $AlCl_3 \cdot 2H_2O = 2$ gm and $Gd_2O_3 = 0.075$ gm.

In K_2NaAlF_6 , RE^{3+} ions could replace K^+ as well as Na^+ sites but calculations were done similar to K_2LiAlF_6 to avoid any kind of disparity.

3 Characterizations

"X-ray diffraction patterns were recorded on a Rigaku MiniFlex II diffractometer. The scanning electron microscopy (SEM) images were taken using ZEISS EVO MA 10 VPSEM. Energy dispersive spectroscopy (EDS) measurements were carried out on EDS Model OXFORD INCA ENERGY 250 system. Dynamic light scattering (DLS) measurement was done on Zetasizer Nano Series (Nano-S) Particle Size Analyzer.

PL spectra were studied using a Hitachi F-7000 spectrofluorimeter in the range of 200–700 nm, with 1–1 nm spectral slit widths. PMT voltage was set at 700 V during scanning of excitation and emission spectra with a rate of 240 nm/min. Lifetime measurements were also carried out on the same

instrument by keeping scanning time range up to 20 ms with chopping speed of 40 Hz. CIE chromaticity coordinates were obtained by using GoCIE software. All the measurements were carried out at room temperature."

4 Results and discussion

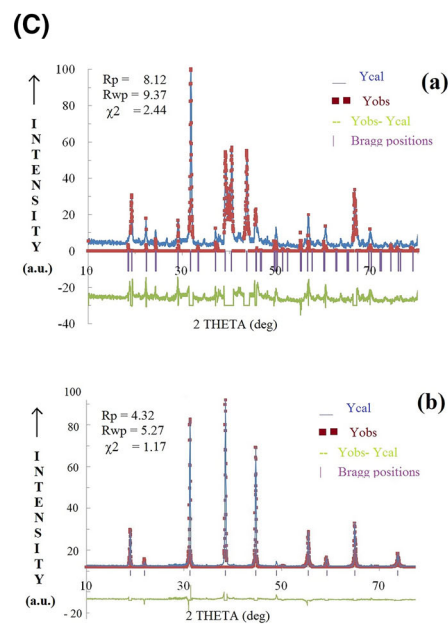
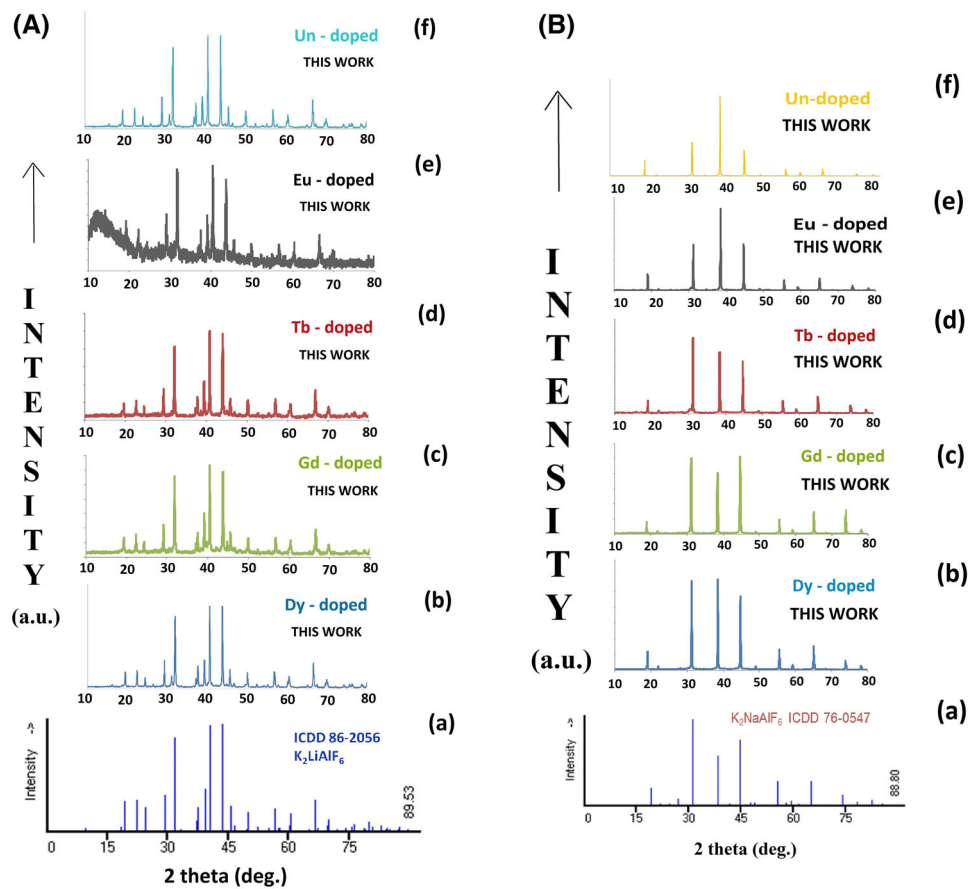
4.1 Phase confirmation and morphological analysis

Figure 1A, B show the XRD comparison of our doped- samples with the standard ones. In order to confirm the formation of the pure phase desired compounds in our sample, XRD was taken for all the RE^{3+} -doped samples. XRDs were taken for 1 mol % dopant concentration. XRDs of un-doped samples were also considered for better comparison. Since, all the XRD patterns are taken for 1% doping concentration, 1% impurity does not make any appreciable changes in the lattice parameters and hence, XRD's of all the samples with different dopants came out to be identical to that of their representative un-doped sample.

It can be clearly seen from the Fig. 1A, B that pure phase compounds K_2LiAlF_6 and K_2NaAlF_6 have been successfully formed in our samples. A HT phase form is always formed during precipitation of K_2LiAlF_6 whereas K_2NaAlF_6 forms in cubic form through present synthesis method (same as seen in our previous studies as well) [16, 17]. XRD patterns of all the samples match well with ICDD 86-2056 for K_2LiAlF_6 and with ICDD 76-0547, in case of K_2NaAlF_6 . Some extra lines of very low-intensities in K_2LiAlF_6 -phase observed are due to the un-reacted constituents (chlorides) remained un-washed during filtration in our samples. Detailed structural studies on both the luminescent-hosts have also been summarized and discussed in our past publications.

To confirm the formation of phase-pure compounds during precipitation synthesis Rietveld refinement was performed. Figure 1C represents refinement for (a) K_2LiAlF_6 and (b) K_2NaAlF_6 —hosts. The XRD data were refined using the FullProf suite software in which the least square refinement weighting model was used and the fitted data were refined to space group R-3 m. The final results converge to the residual factors of R_p : 8.12% & R_{wp} : 9.37% indicating a good quality of refinement. The

Fig. 1 **A** Comparison between XRD patterns of K_2LiAlF_6 with different dopants, (a) KLAf-(Standard), (b) KLAf:Dy(1 mol%), (c) KLAf:Gd(1 mol%), (d) KLAf:Tb(1 mol%), (e) KLAf:Eu(1 mol%) and (f) KLAf –(Pure); **B** Comparison between XRD patterns of K_2NaAlF_6 with different dopants, (a) KNAf-(Standard), (b) KNAf:Dy(1 mol%), (c) KNAf:Gd(1 mol%), (d) KNAf:Tb(1 mol%), (e) KNAf:Eu(1 mol%) and (f) KNAf –(Pure); **C** Rietveld refinement performed on undoped (a) K_2LiAlF_6 & (b) K_2NaAlF_6 host samples



goodness of fit was $\chi^2 = 2.44$. Results of Rietveld refinement are shown in Fig. 1C(a), confirming a hexagonal phase for K_2LiAlF_6 . Refined Cell parameters came out to be, $a = 5.6290 \text{ \AA}$, $b = 5.6290 \text{ \AA}$, $c = 27.6829 \text{ \AA}$, coinciding well with the ICDD (86-2056) data. Similarly, The XRD data were refined for K_2NaAlF_6 and the fitted data were refined to space group Fm-3 m. The final results converge to the residual factors of Rp: 4.32% and Rwp: 5.27% indicating good quality of refinement. The goodness of fit was $\chi^2 = 1.17$. Results of Rietveld refinement are shown in Fig. 1C(b). A Cubic phase was confirmed for K_2NaAlF_6 and the Refined Cell parameters are $a = b = c = 8.1225 \text{ \AA}$, coinciding well with the ICDD (76-0547) data.

Further to confirm the formation of desired compounds in our Gd-doped samples, separate XRPD are conducted on various Gd^{3+} - concentrations, as well. It is evident from the both Fig. 2A, B that XRD lines obtained for various $Gd^{3+}-K_2LiAlF_6$ & $Gd^{3+}-K_2NaAlF_6$ samples also match very well with their respective ICDD data though there are small variations in relative intensities.

Figures 3, 4 show the SEM images of K_2LiAlF_6 & K_2NaAlF_6 compounds, respectively. SEM images taken for 20, 10, 2 and 1 μm scale; show bigger particles of micrometer range. Most of the particles are of irregular shapes and are nearly around 2 μm in size. Particles in KLAf appear agglomerated but when focussed at 2 μm level (Fig. 3b), few particles with smaller dimension than 1 μm also appear.

KNAf SEM images illustrate interesting flowery-type flakes, growing out of octahedral-shaped particles. Most of these octahedral-shaped particles lie within the 2–4 μm range. EDS analysis was also done for the same (Fig. 5).

Figure 5 gives the results of EDS study done on K_2NaAlF_6 , as EDS was not performed on these compounds earlier. Table 1: gives the comparison between the experimentally observed values to the calculated ones, as a result of EDS analysis. The observed atomic % values for K, Na, Al and F were found to be nearly equal to the values attained through calculations. Hence, EDS results show that K_2NaAlF_6 has been formed in with elements in anticipated ratios. EDS was performed on an undoped sample.

EDS cannot be executed for KLAf crystals. Due to the presence of 'Li' in the host, proper study of elemental composition is not possible.

DLS study was carried out in order to find the exact range of particle size in as-prepared samples. Figure 6 exhibits the particle size distribution for KLAf crystals. It can be seen that the maximum number of particles are of the size from 1 to 4 μm . This was confirmed by the SEM images also.

Details of the DLS measurement and analysis are discussed below:

The Z-Average Size i.e. the peak at which size of maximum number of particles, formed through precipitation method lies at 2467 d.nm. The polydispersity index (PDI) was 0.248 for our sample solution. International standards organizations (ISOs) has standardized the PDI values below 0.7 that are considered to be good for DLS measurements. There was only one peak recorded with highest value at 2467 d.nm and that too is with 100% composition.

There is a possibility of smaller particles than 1 μm , may be present in the samples (as depicted in SEM images) but they are expected to be very few in percentage.

Unlike other characterizations, for DLS measurements sample was prepared by dispersing 0.1/0.2 gms of sample in 10 ml of solvent (preferably D.I. water for fluorides). Sonication for at least 90 min. is necessary, before the measurements. All other measurements were done on as it is powdered samples.

Hence, XRDs confirms the formation of desired phases, SEM and DLS measurements helps in estimating the exact particle sizes, whereas EDS was done to validate the formation of expected elpasolite-formula A_2BMF_6 in our samples.

4.2 Photoluminescence (PL) and decay kinetics

Photoluminescence studies were done for Gd^{3+} , Tb^{3+} , Dy^{3+} and Eu^{3+} rare earth dopant ions in both KLAf and KNAf compounds. Among these results of Gd^{3+} appear most promising. Five samples of Gd^{3+} (concentrations 0.5, 1, 2, 3 and 5 mol %) were prepared and investigated. Figure 7a shows PL emission spectra for different Gd^{3+} conc. in KLAf. Figure 7b displays conc. Vs PL intensity graph. PL intensity due to Gd^{3+} as impurity in KLAf tends to increase monotonously with increase in dopant concentrations from 0.5 to 5%. The graph Fig. 7b suggests that it keeps on increasing up to the 5% conc. but can saturate afterwards, due to quenching effects. Figure 8a shows the excitation spectra for respective

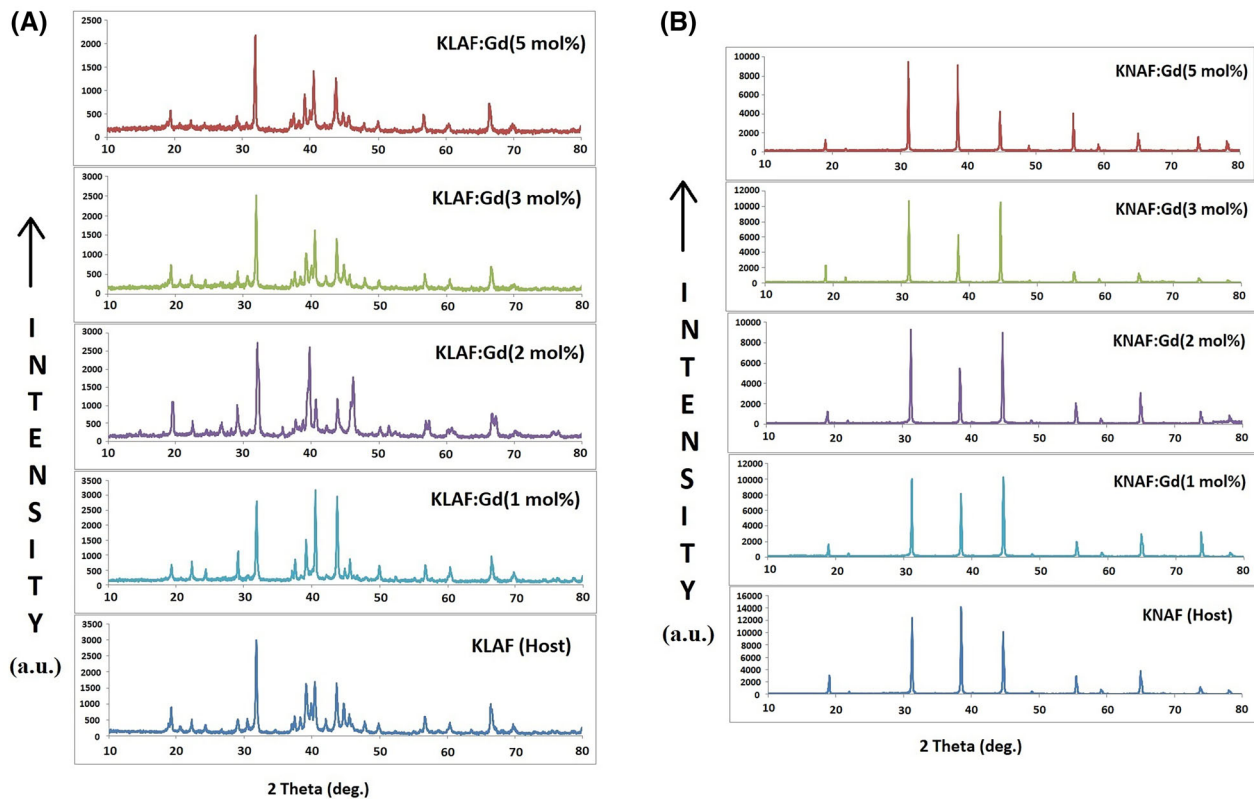


Fig. 2 A XRD comparison of various concentrations of gadolinium in K_2LiAlF_6 with phase-pure host; B XRD comparison of various concentrations of gadolinium in K_2NaAlF_6 with phase-pure host

PL emissions for various Gd^{3+} conc. in KLA:F. To show the proper shape and structure, more detailed excitation spectra is drawn in Fig. 8b displaying its responsible spectra on it. Excitation spectrum for 5% Gd^{3+} conc. was not taken because of similar nature of PL excitation for every sample.

All the Gd^{3+} PL emission spectra were taken for 272 nm excitation wavelength, whereas excitations were observed for 310 nm emission wavelength. This is the characteristic emission spectra for Gd^{3+} ions in any host. The emission as well as excitation spectrum consists of very sharp and narrow peaks. Even slight variation from these expected wavelengths during measurements can lead to abrupt decrease in PL intensities. Excitation results from the f-f transitions from ground state energy level $^8S_{7/2}$ to various higher energy state multiplets 6I_j and 6D_j . Strongest peak at 272 nm corresponds to $^8S_{7/2} \rightarrow ^6I_1$, whereas weaker ones belong to $^8S_{7/2} \rightarrow ^6D_j$. Similarly, emission spectrum comprises of two emission peaks, one at 305 nm corresponds to $^6P_{5/2} \rightarrow ^8S_{7/2}$ and the other major one at 310 nm is due to $^6P_{7/2} \rightarrow ^8S_{7/2}$ transition

[29–31]. A close look at the excitation spectra reveals detailed structure with more noticeable transition lines. These may be assigned as 243, 245, 252, 272, 275 and 278 nm corresponding to transitions from $^8S_{7/2}$ $^6D_{5/2}$, $^6D_{7/2}$, $^6D_{9/2}$, $^6I_{15/2}$, $^6I_{13/2}$, $^6I_{11/2}$ and $^6I_{9/2}$, $^6I_{7/2}$ (Fig. 8b) [32].

Figure 9a shows the time (in ms) Vs normalised Intensity, decay curves for KLA:F:Gd $^{3+}$ (0.5, 1, 2, 3, 5 mol %). The decay curves for all the Gd^{3+} conc. have been plotted on the same graph to understand the effect of variation in dopant conc. on the lifetime (τ). The direction of the arrow indicates that lifetime decreases with increasing Gd^{3+} conc. This is due to increased energy transfer among Gd^{3+} ions at higher concentrations [33].

Further, the fitting of the data points portrays that the above decay kinetics can be expressed in the following first-order exponential equation:-

$$I = I_0 e^{-t/\tau} \quad (1)$$

where, I and I_0 represent the luminescence intensities at time t & 0, respectively. Lifetime (τ) is deduced as mean lifetime when the value of I/I_0 reduces to its

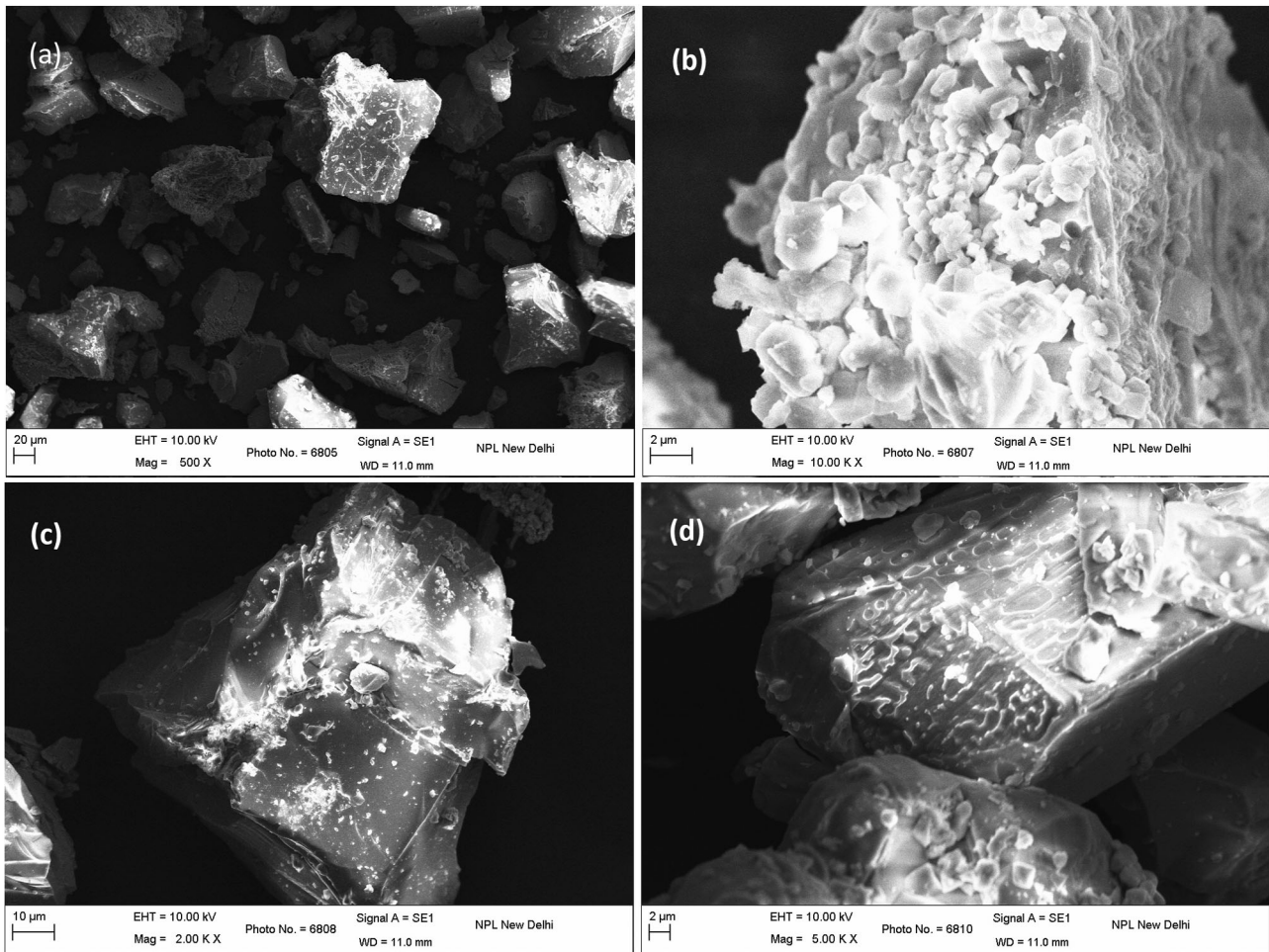


Fig. 3 SEM images of K_2LiAlF_6 (pure) at different resolutions **a** 20 μm , **b** 2 μm , **c** 10 μm and **d** again, at 2 μm

70% of its actual value (i.e. when I/I_0 comes to $1/e \approx 0.3$ (approx) times its initial value).

Figure 9b depicts the picture more clearly. The $\ln(I/I_0)$ versus Time (ms) graph results in the linear fitting of data points and helps in distinguishing the decay kinetics more distinctly. It clearly displays the lifetime due to Gd^{3+} (0.5%) is, $\tau = 7.7$ ms, whereas it decreases precisely to $\tau = 4.6$ ms for higher conc. of Gd^{3+} (5%) due to increase in $Gd^{3+}Gd^{3+}$ energy transfer.

Figure 9c shows a graph between mean lifetime deduced with the help of Eq. (1) Vs Gd^{3+} conc. Data points fit more perfectly with the logarithmic scale which in turn demonstrates the same exponentially decreasing behaviour as it was observed for the lifetime decay curves. ' τ_R ' i.e. intrinsic radiative lifetime was found to be equal to 6.455 ms, from the graph. Further, value of τ_R is useful in calculating quantum

efficiency (\emptyset)% and non-radiative rates(A_{nR}) with the help of following equations [34, 35]:-

$$\emptyset = \frac{\tau_0}{\tau_R} \tag{2}$$

$$A_{nR} = \frac{1}{\tau_0} - \frac{1}{\tau_R} \tag{3}$$

where, τ_0 represents the mean lifetime at a particular dopant conc. Table 2 displays the calculated values of \emptyset % and A_{nR} for various Gd^{3+} conc.

It can be clearly seen from the Table 2 that the internal quantum efficiency (\emptyset %) decreases continuously with increasing Gd^{3+} conc. whereas an increase in the values of non-radiative rates (A_{nR}) is observed for the same.

Figure 10 shows the PL emission and excitation spectra for $KLAF:Tb^{3+}$ (1 mol%). Emission was taken at 285 nm excitation wavelength and excitation was scanned for 543 nm emission wavelength. The

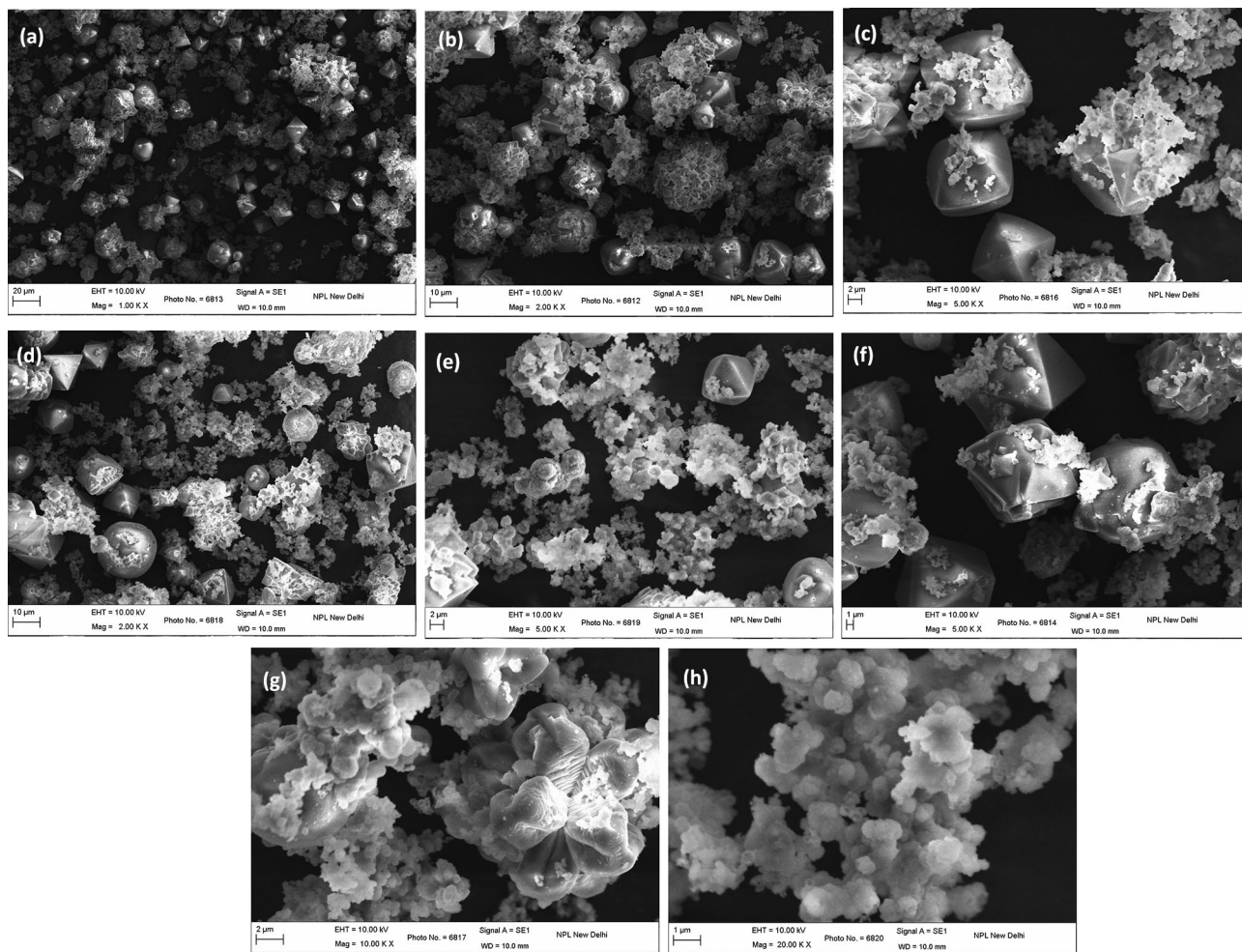


Fig. 4 SEM images of K_2NaAlF_6 (pure) at different resolutions **a** 20 μm , **b** 10 μm , **c** 2 μm , **d** 10 μm , **e** 2 μm , **f** 1 μm , **g** 2 μm and **h** 1 μm

excitation spectrum consists of f-f transitions from the ground state 7F_6 to the different excited states of Tb^{3+} and produces excitation peaks at 317 nm (5D_0), 340 nm (5G_2), 351 nm (5D_2), 357 nm (5G_5), 368 nm (5G_6) and 377 nm (5D_3) [36]. The overall emission spectrum originates from the f-f transitions between levels of $4f^8 Tb^{3+}$ electronic configuration and consists of the blue region $^5D_4^7F_6$ (490 nm) and the green region $^5D_4^7F_5$ (543 nm), as well as the red-region $^5D_4^7F_4$ (587, 590 nm), $^5D_4^7F_3$ (622 nm). Few small emission peaks are also visible before 480 nm and are due to $^5D_3-^7F_j$ ($J = 2, 3, 4, 5$) transitions, whereas the intense ones correspond to $^5D_4-^7F_j$ ($J = 3, 4, 5, 6$) [31]. The 543 nm peak has the strongest emission intensity [37]. The excitation bands between the 230–300 nm range are due to f-d i.e. $4f^8 4f^7 5d^1$ transitions and those falling in the 300–400 nm range, owe to the $4f^8$ [38].

Figure 11 displays emission and excitation PL spectra of $KLaF_6:Dy^{3+}$ (1 mol%). Emission was scanned from 470 to 620 nm and two emission peaks (one at 481 and other at 573 nm) were recorded for 350 nm excitation. The intensity of excitation spectra appears lesser than its respective emission intensities could be because it was recorded for the less intense 573 nm peak. Though the intensities were very weak for this phosphor, we are successful in recording some of the important peaks of Dy^{3+} characteristic spectra. Usually, the Dy^{3+} excitation spectrum consists of peaks at 326, 352, 366, 389, 426, 452 and 468 nm. Among these peaks at 326, 351, 363 and 387 nm are observed in our sample for 573 nm emission. 351 nm is considered to be the most prominent peak of the spectrum and mostly used as excitation due to its applications in solid-state lighting [39]. These peaks arise due to excitation from the ground state $^6H_{15/2}$ to excited

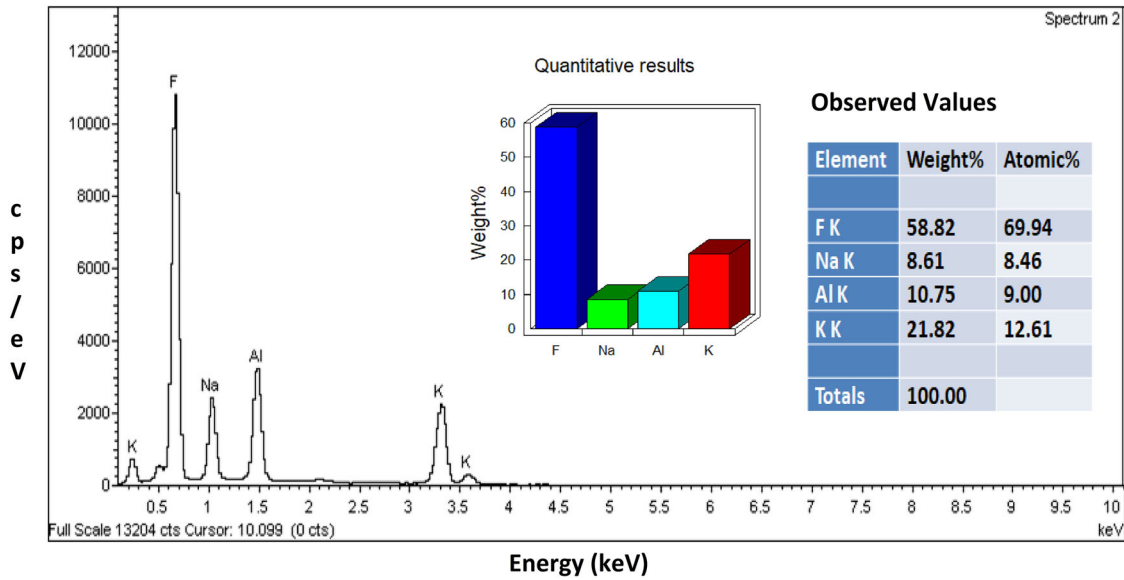


Fig. 5 Energy dispersive X-ray (EDAX) analysis of K_2NaAlF_6 —pure compound

Table 1 Observations of EDS analysis done on K_2NaAlF_6 compound

Atomic %	K	Na	Al	F
Observed values	12.61	8.46	9.00	69.94
Calculated values	20	10	10	60

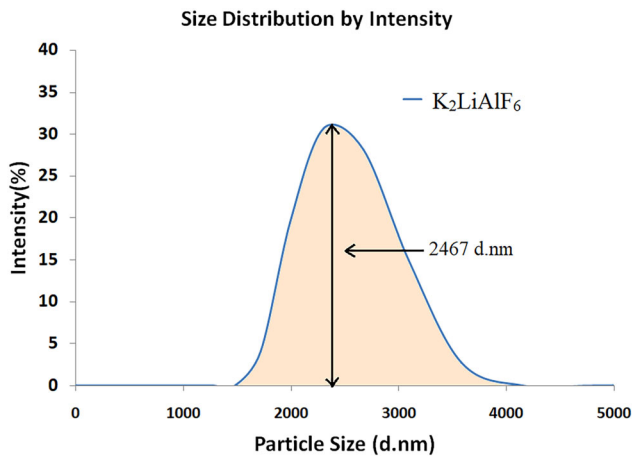


Fig. 6 Dynamic light scattering (DLS) Analysis done on pure— K_2LiAlF_6 estimates particles of micro-level size

states ${}^6P_{3/2}$, ${}^6P_{7/2}$, ${}^6P_{5/2}$, ${}^4I_{13/2}$, respectively. Emission spectrum observed contains two intense peaks, one in blue region at 481 nm due to ${}^4F_{9/2}$ ${}^6H_{15/2}$ transition and another in yellow at 573 nm resulting from ${}^4F_{9/2}$ ${}^6H_{13/2}$ transition [40]. In our case, the 481 nm

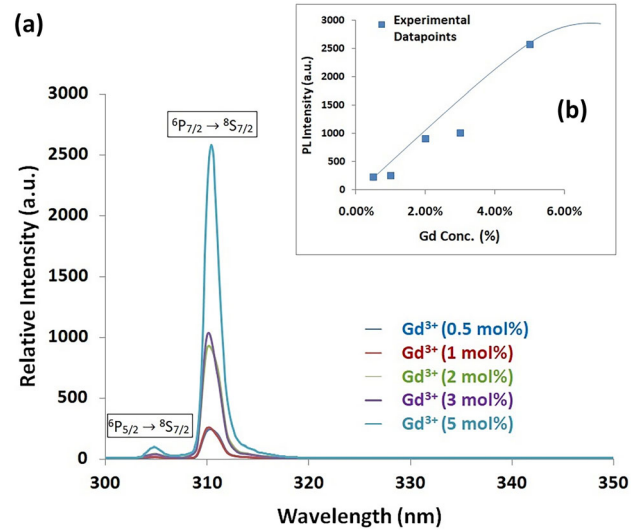


Fig. 7 Shows **a** PL emission spectra observed for excitation wavelength at $\lambda_{ext} = 272$ nm for different concentrations of Gd^{3+} ion in K_2LiAlF_6 . Corresponding transitions responsible are also shown on their respective emission peaks, **b** concentration quenching graph drawn between the PL intensity versus Gd % concentration

emission appears more intense than the other one. This can happen when the Dy^{3+} ion occupies the site of higher symmetry within the crystal lattice [41].

Figure 12 exhibits PL emission and excitation spectra for $KLAF:Eu^{3+}(1\text{ mol}\%)$. Emission was recorded for 390 nm excitation, whereas excitation was scanned for 590 nm emission wavelength. Emission spectra by trivalent europium ion consists

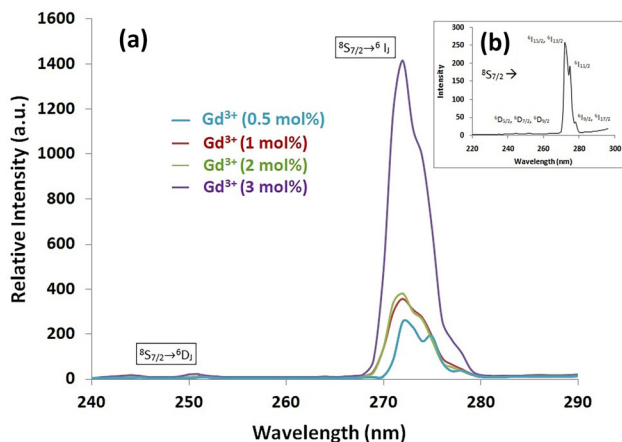


Fig. 8 Shows **a** PL excitation spectrum taken for emission wavelength at $\lambda_{em} = 310$ nm for $K_2LiAlF_6:Gd^{3+}$. Corresponding transitions responsible are also shown on their respective excitation peaks, **b** shows more detailed nature of the excitation spectra

of many sharp lines. The prominent peaks around 600 nm are assigned to 5D_J 7F_J transitions, where $J = 0, 1, 2, 3, 4, 5, 6$ when excitation of 395 to 398 nm is given to the sample. The two intense peaks observed in emission spectrum of our sample are at 592 and 614 nm and are attributable to the $^5D_0 \rightarrow ^7F_1$ & $^5D_0 \rightarrow ^7F_2$ transitions in Eu^{3+} ions. The excitation peaks at 393 and 464 nm having comparatively greater intensity correspond to $^7F_0 \rightarrow ^5L_6$ and $^7F_0 \rightarrow ^5D_2$ transitions [42]. The peaks with their respective transitions are labelled on the Fig. 12, for better clarity.

Similar types of results were observed for the compound K_2NaAlF_6 when doped with RE^{3+} ions as activators. Figure 13a shows Gd^{3+} -emission spectra for all five concentrations in KNAF host lattice. Same as observed for KLAf, the PL intensity keeps on increasing monotonously up to 5 mol % dopant

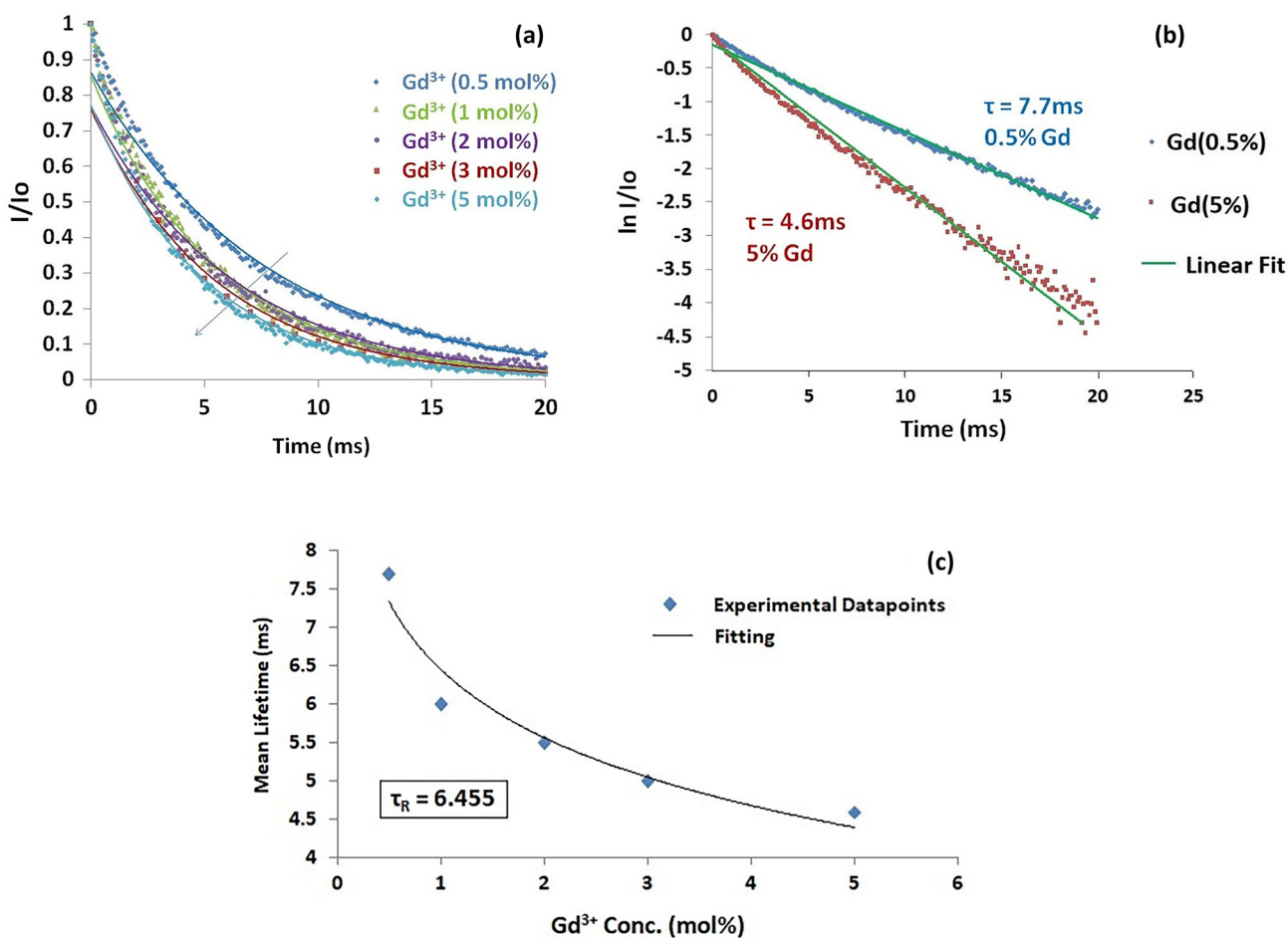


Fig. 9 Displays **a** lifetime decay curves recorded for various concentrations of Gd^{3+} doped K_2LiAlF_6 samples fitted with logarithmic scale, taken at 272 nm excitation for 310 nm emission,

b $\ln(I/I_0)$ with respect to Time(ms) plot reveals linear fitting of datapoints, **c** exponential decrease in the lifetime value with respect to dopant concentration

Table 2 Calculated quantum efficiency (\varnothing) % and non-radiative rates (A_{nr}) values for KLAf:Gd samples

Gd ³⁺ conc. (mol %)	Mean lifetime (ms)	\varnothing (%)	A_{nr} in (s ⁻¹) (Non-radiative rates)
1	6	93	11.8
2	5.5	85	26.9
3	5	77	45.1
5	4.6	71	62.5

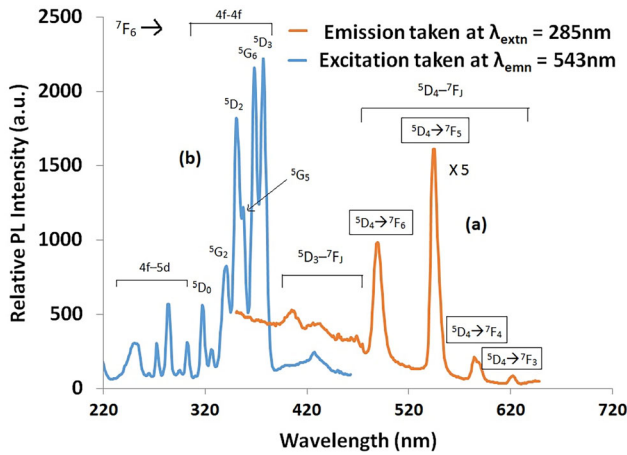


Fig. 10 Plots PL emission and excitation intensity versus wavelength graph for K₂LiAlF₆:Tb³⁺(1 mol%) phosphor. Responsible transitions are marked on all the visible peaks. **a** Emission taken at 285 nm excitation wavelength and **b** excitation scanned for 543 nm emission

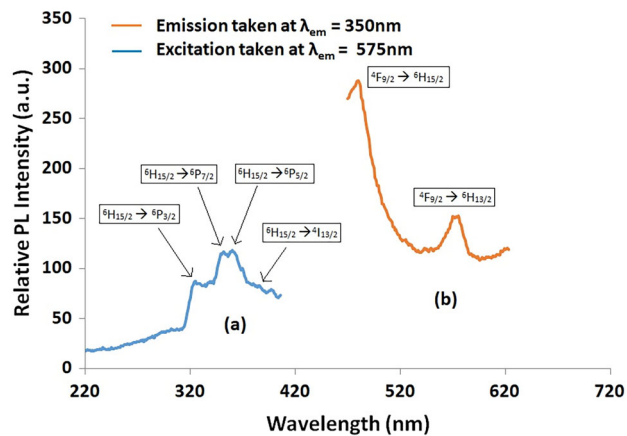


Fig. 11 Shows PL emission and excitation spectra for K₂LiAlF₆:Dy³⁺(1 mol%) with responsible transitions marked on the selective intense peaks. **a** Excitation scanned for 575 nm emission wavelength and **b** emission taken at 350 nm excitation wavelength

concentration (Fig. 13b). It is expected to saturate beyond this point due to dopant ion's concentration quenching. Emission was taken for 272 nm excitation and Fig. 13c excitation was analysed for 310 nm

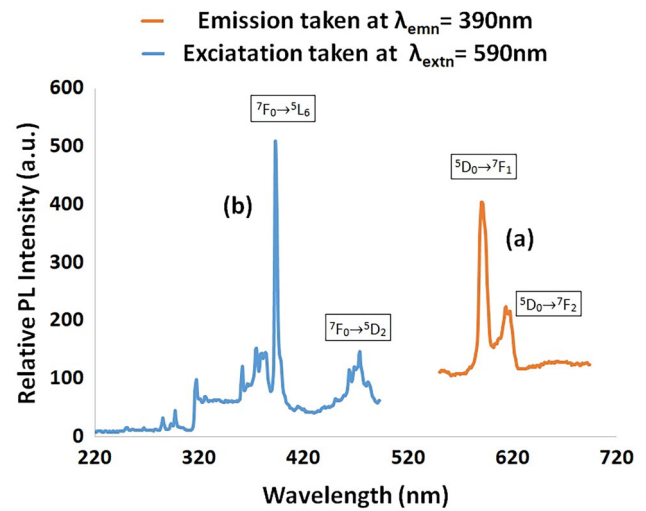
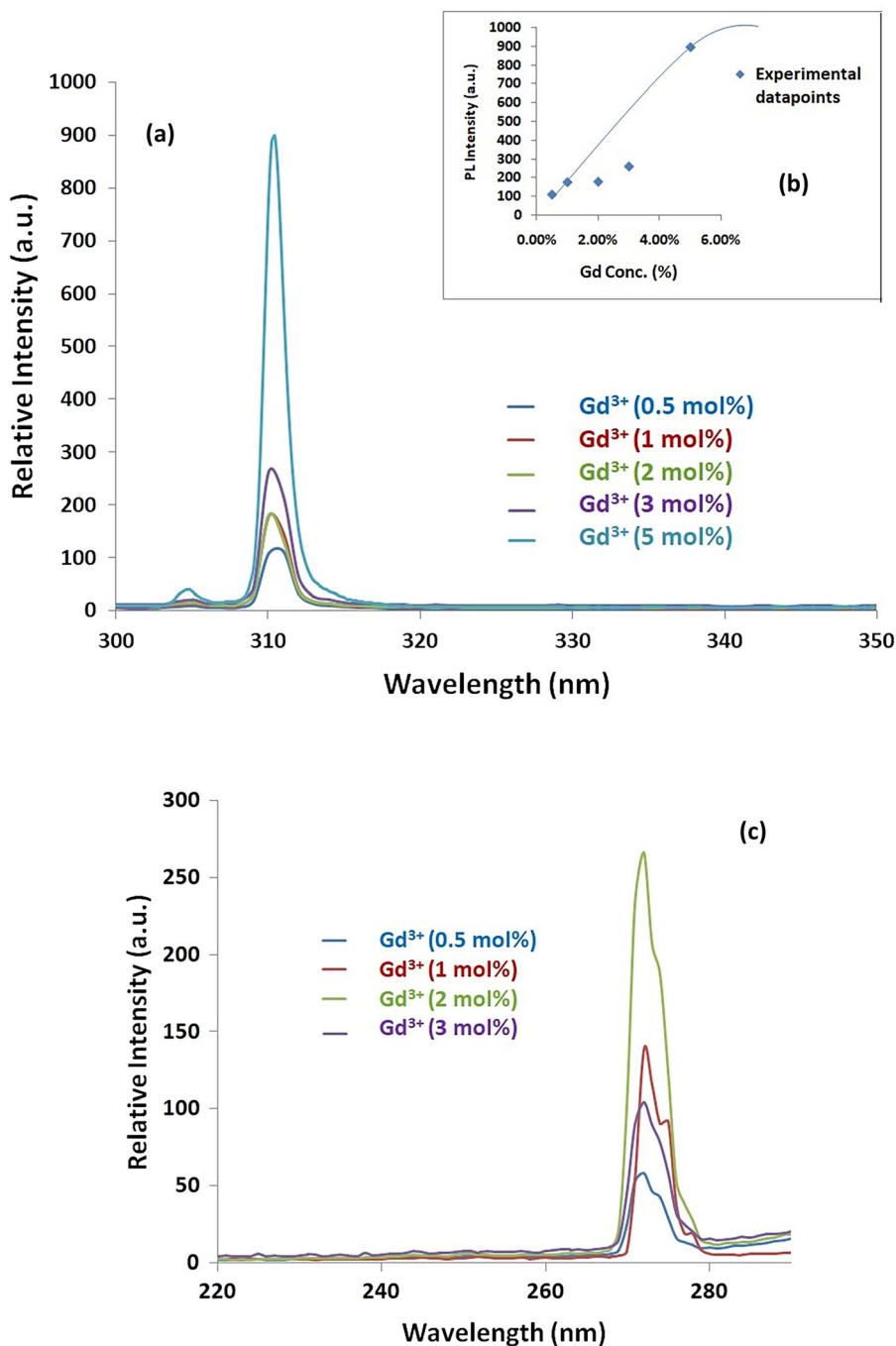


Fig. 12 Shows PL emission and excitation spectra for K₂LiAlF₆:Eu³⁺(1 mol%) with responsible transitions marked on the selective intense peaks. **a** Emission taken at 390 nm excitation wavelength and **b** excitation scanned for 590 nm emission wavelength

emission for Gd³⁺ ions in KNAF. Figure 14a shows the variation of normalized intensity with respect to time, for five Gd³⁺ concentrations in KNAF [KNAF:Gd³⁺ (0.5, 1, 2, 3 and 5%)]. A continuous decrease in the lifetime of the PL emission with increase in Gd³⁺ conc. was observed in KNAF host also. The direction of arrow is marked on the figure to demonstrate such behaviour. For better perception of this phenomena, a plot between ln(I/I₀) with respect to time (in ms) (Fig. 4b) has been employed, which clearly illustrates the difference between the lifetime observed for Gd³⁺ (0.5 mol %) compared to (5 mol %) conc. It is perspicuously visible from the Fig. 14b that on adding impurity Gd³⁺ to KNAF from 0.5 to 5% concentration, Lifetime (τ) tends to decrease from the value of 12.3 ms to 4.1 ms remarkably. It was evident from the above lifetime variation graphs that similar types of results have been noticed for the KLAf compound as well. Values of mean lifetime for every concentration have been depicted from the Eq. (1). The first-order nature of the exponential

Fig. 13 Shows **a** PL emission spectra scanned for excitation wavelength at $\lambda_{\text{ext}} = 272$ nm for different concentrations of Gd^{3+} ion in K_2NaAlF_6 , **b** concentration quenching graph drawn between the PL intensity versus Gd^{3+} % concentration, **c** PL excitation spectrum taken for emission wavelength at $\lambda_{\text{em}} = 310$ nm for $\text{K}_2\text{NaAlF}_6:\text{Gd}^{3+}$



equation depicts the existence of single luminescence center in the coordination complex. Figure 14c helps in understanding the behaviour of mean lifetime variations with increase in dopant concentration. Logarithmic plot fits the data points best and suggests the same exponential decrease as was observed for the decay curves with respect to Gd^{3+} conc. The value of ' τ_R ' was found to be equal to 8.876 for fitting equation. Further as done for $\text{KLaF}_6:\text{Gd}^{3+}$, ' τ_R ' is used

to calculate quantum efficiency (ϕ) % and non-radiative rates (A_{nr}) from Eqs. (2), (3). Table 3 lists the obtained quantities of quantum efficiency (ϕ)% and non-radiative rates (A_{nr}) with increase in Gd^{3+} concentration along with its mean lifetime values.

A steep decrease in the calculated value of ϕ % is observed while on contrary, a continuous increase in non-radiative transition rates was found for the same. This could be explained as due to more number of

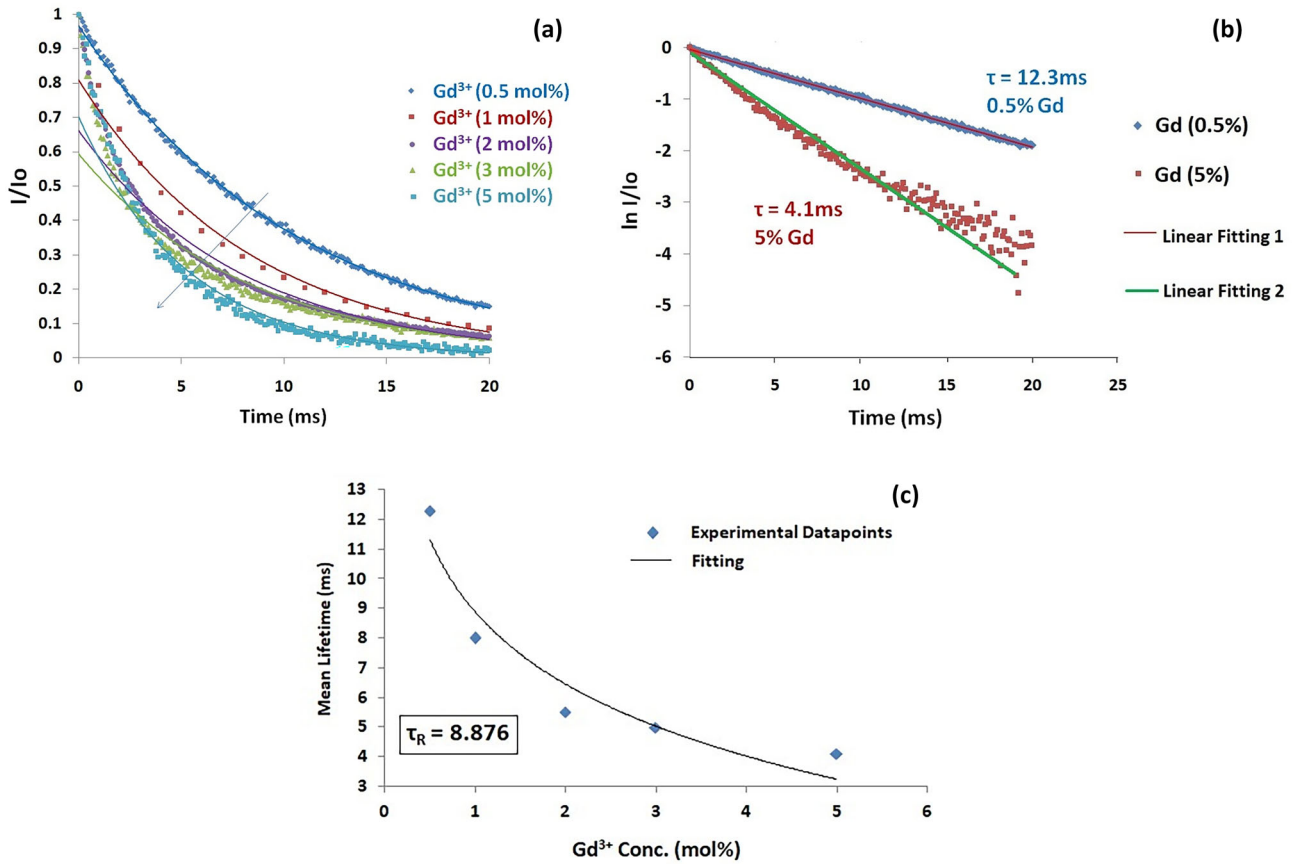


Fig. 14 Displays **a** lifetime decay curves recorded for various concentrations of Gd^{3+} doped K_2NaAlF_6 samples fitted with logarithmic scale, taken at 272 nm excitation for 310 nm emission, **b** $\ln(I/I_0)$ with respect to Time (ms) plot reveals linear fitting of datapoints, **c** exponential decrease in the lifetime value with respect to dopant concentration

Table 3 Calculated quantum efficiency (\emptyset) % and non-radiative rates (A_{nR}) values for KNAF:Gd samples

Gd ³⁺ conc. (mol%)	Mean lifetime(ms)	\emptyset %	A_{nR} in (s ⁻¹) (Non-radiative rates)
1	8	90	12.3
2	5.5	62	69.1
3	5	56	87.3
5	4.1	46	131.2

non-radiative decays with increase in number of dopant ions. At higher dopant concentrations, phonon energy transfer prevails due to proximity of dopant ions in host lattices which in turn produces surge in inefficient energy transfers [43]. Quantum efficiency measured here can be referred to as internal (QE) because it did not include transmittance and reflection losses during calculations [44].

Figure 15a–c give the characteristic spectra for KNAF samples containing Tb^{3+} , Dy^{3+} and Eu^{3+} as

RE^{3+} activators for 1 mol % concentration, respectively. Almost similar type of excitation and emission bands were observed for RE^{3+} -activated KNAF as were recorded for KLAf. The positions of all major as well as minor peaks are same and the electronic transitions responsible for emergence of these spectrums have been already discussed in details for KLAf. Although, the intensity of trivalent dysprosium-doped KLAf was very low and posed challenges during measurements, KNAf:Dy³⁺ was found

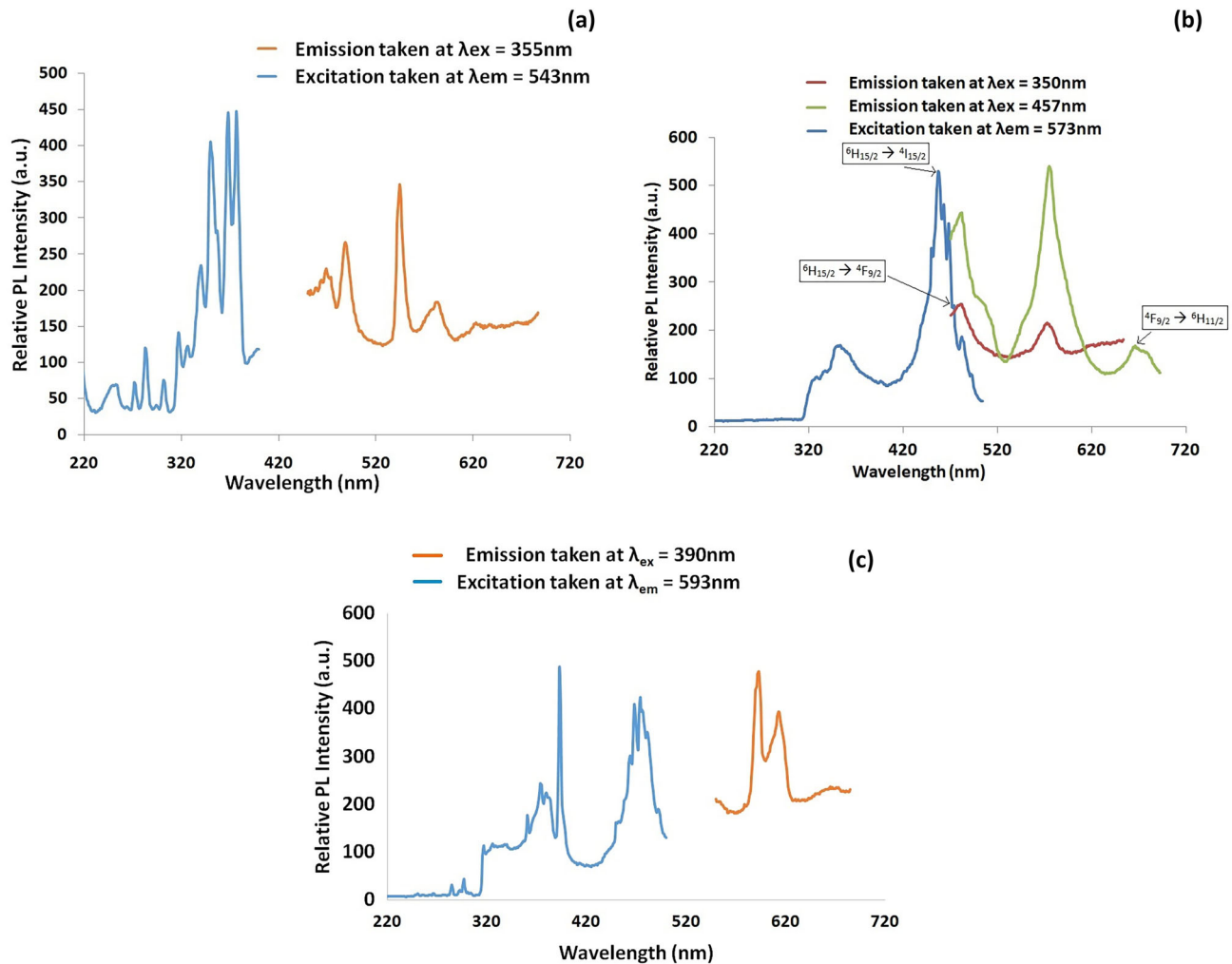


Fig. 15 Shows **a** PL spectra of $\text{K}_2\text{NaAlF}_6:\text{Tb}^{3+}$ (1 mol%), emission taken at 355 nm excitation wavelength and excitation scanned for 543 nm emission wavelength. **b** PL spectra of $\text{K}_2\text{NaAlF}_6:\text{Dy}^{3+}$ (1 mol%), emission taken at 350 and 457 nm

excitation wavelength and excitation scanned for 573 nm emission wavelength. **c** PL spectra of $\text{K}_2\text{NaAlF}_6:\text{Eu}^{3+}$ (1 mol%), emission taken at 390 nm excitation wavelength and excitation scanned for 593 nm emission wavelength

to be relatively better phosphor. This time we were successful in recording some other bands of the spectrum, marked individually (which were not seen for $\text{K}_2\text{NaAlF}_6:\text{Dy}^{3+}$) on the Fig. 15b. Apart from the strong peaks of around 481 and 575 nm in emission region, a small low intensity peak at 647 nm (due to ${}^4\text{F}_{9/2} \rightarrow {}^6\text{H}_{11/2}$ transition) is also visible in a sample when excited by a 457 nm wavelength [41]. Sharp lines are not clearly visible in the excitation, instead a broad band appearing from 300 to 400 nm consisting of few low intensity peaks at 326, 354 and 363 nm are visible. These lines have been already recorded and

explained in depth for $\text{K}_2\text{NaAlF}_6:\text{Dy}^{3+}$. The excitation spectra taken beyond 400 nm is very noisy but still two excitation peaks at 457 and 474 nm are distinguishable. Excitation peak at 457 nm arises due to ${}^6\text{H}_{15/2} \rightarrow {}^4\text{I}_{15/2}$, whereas 474 nm corresponds to ${}^6\text{H}_{15/2} \rightarrow {}^4\text{F}_{9/2}$ [40].

4.3 Atomic substitution and coordination

Though atomic structures with proper coordination have been already discussed in our previous publications, value of radius percentage discrepancy (D_r)

has been calculated for every possible substitution specifically this time. In both $K_2Li/NaAlF_6$ there are 3–3 cationic sites that can be replaced by rare earth ions as an activators:- for e.g. in KLAf the first one is 'Al³⁺' due to charge compensation, second one is 'Li⁺' & the third one is 'K⁺' due to comparable ionic size. Al³⁺ ions size is too small to be replaced by Gd³⁺, Tb³⁺, Eu³⁺ or Dy³⁺ ions.

In K_2LiAlF_6 Gd³⁺/Tb³⁺/Eu³⁺/Dy³⁺ may substitute K⁺ site due to comparable ionic sizes. Again, Li⁺ is also too small to be got replaced.

In K_2NaAlF_6 Gd³⁺/Tb³⁺/Eu³⁺/Dy³⁺ may substitute K⁺/Na⁺ site due to comparable ionic sizes. Let us find out the exact possibility for substitution by calculating radius percentage discrepancy (D_r) value for every ion.

The radius percentage discrepancy (D_r) is used to determine the substitution between the doped RE³⁺ ions and the probable site of substituted ions in their respective hosts, which can be calculated through the following formula [45]:

$$D_r = \frac{R_s(\text{CN}) - R_d(\text{CN})}{R_s(\text{CN})} \times 100\% \quad (4)$$

where CN denotes the abbreviation of coordination number, R_s represents the radius of the substituted ions, R_d is the radius of doped RE³⁺ ions, and D_r is the different radius percentage values. For perfect substitution, D_r value should be less than 30%.

Coordination number(CN) in KL/NAF, for K⁺ is 12, Li⁺/Na⁺ is 6 and for Al³⁺ is also 6.

In K_2LiAlF_6 , K⁺ is most likely to get replaced/substituted due to its comparable ionic size, as illustrated by the table below (Table 4):-

For all other substitutions, D_r values are coming out to be unacceptable due to comparatively smaller ionic radii sizes of Li⁺ and Al³⁺. Even though Al³⁺ is expected to be perfect for ionic replacement due to similar valency, but it's too small ionic radius produces undesirable D_r values. Hence, possibility of K⁺ substitution looks more convincing.

Similarly, D_r can be calculated for K_2NaAlF_6 for all four RE³⁺ ions. Due to small size of Al³⁺ ion, it is ruled out at the first step itself. Also almost similar results as such observed for KLAf:RE³⁺ were obtained for K⁺ substitution in K_2NaAlF_6 . Therefore, the table below gives the calculated values for ' D_r ' when RE³⁺ ions are supposed to substitute Na⁺ ions (Table 5).

Therefore for KNAf host, from the above table and calculated ' D_r values' Tb³⁺ and Eu³⁺ could replace K⁺ ions since the values are coming out to be lesser than 30%, whereas Gd³⁺ and Dy³⁺ can fit easily into the substitutional Na⁺ sites.

4.4 CIE chromaticity coordinates

CIE coordinates (x,y) have been plotted on Commission International De l'Eclairage CIE 1931 colour chromaticity coordinate plane. In order to estimate the applicability of our phosphors on at industrial level, CIE colour coordinates need to be framed out on a colour representing graphical diagram, popularly termed as CIE colour chromaticity coordinate graph. The white region present in the middle of the chromaticity diagram is the epicenter enclosed by Planckian locus. The closure the coordinates of the phosphor lies to this epicenter or within the range of the Planckian locus, are considered as the best white light-emitting phosphors for the application in solid-state lighting. PL emission spectra is required to locate the exact (x,y) colour coordinates on the colourful diagram. For a 100% white light emitter, the both coordinates should have $x = y = 0.3333$ CIE values.

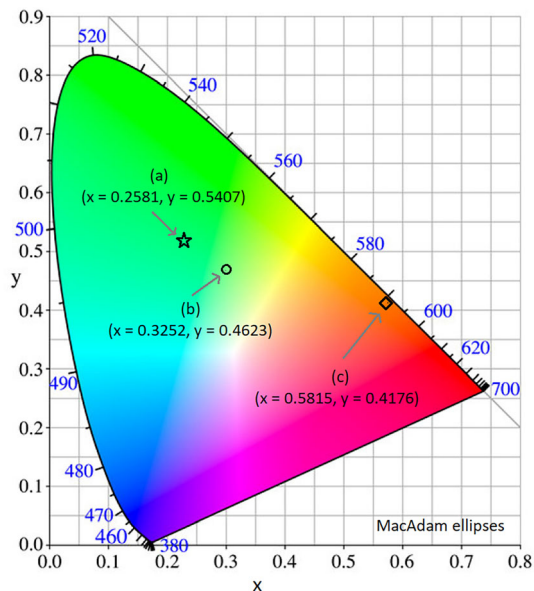
As the colour coordinates can be observed only for the phosphors which emits in visible range (i.e. starting from 380 or 440 nm), coordinates (x,y) have been plotted for all the other phosphors except the one with Gd³⁺-doping. All coordinates were calculated for 1 mol% concentration of RE³⁺. Figure 16a–c display colour-coordinates for Tb³⁺, Dy³⁺, Eu³⁺ -doped KLAf phosphors respectively. Colour

Table 4 Calculation for ' D_r ' value of RE³⁺ ions replacing 'K⁺' ions in KLAf

If Re ³⁺ ions to substitute K ⁺ ions in K_2LiAlF_6 (CN = 12)	Calculated D_r values
Gd ³⁺ K ⁺	32% ≈ 30%
Tb ³⁺ K ⁺	14.49% < 30%
Dy ³⁺ K ⁺	34% ≈ 30%
Eu ³⁺ K ⁺	23.19% < 30%

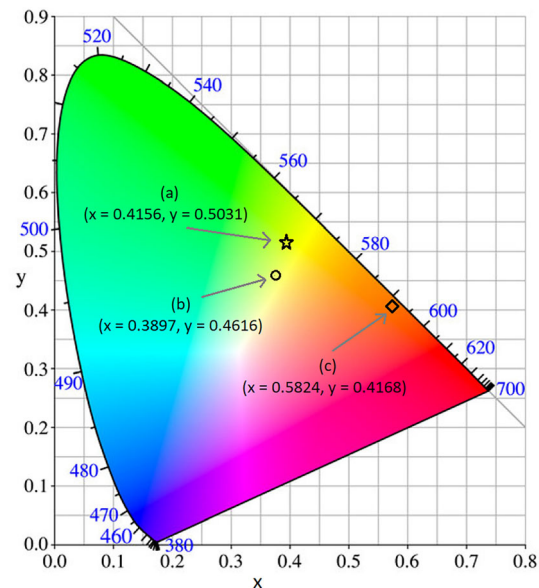
Table 5 Calculation for 'D_r' value of RE³⁺ ions replacing 'Na⁺' ions in KNAF

If RE ³⁺ ions to substitute Na ⁺ ions in K ₂ NaAlF ₆ (CN = 6)	Calculated D _r values
Gd ³⁺ Na ⁺	8.04% < < 30%
Tb ³⁺ Na ⁺	Unacceptable value
Dy ³⁺ Na ⁺	10.78% < 30%
Eu ³⁺ Na ⁺	Unacceptable value

**Fig. 16** CIE chromaticity coordinates(x,y) high-lighted by the star, circle and square marks on the chromaticity diagram for **a** KLAf:Tb³⁺ (1 mol%) phosphor under 285 nm excitation wavelength, **b** KLAf:Dy³⁺ (1 mol%) phosphor under 350 nm excitation wavelength, **c** KLAf:Eu³⁺ (1 mol%) phosphor under 390 nm excitation wavelength

coordinates for KLAf:Tb³⁺ (Fig. 16a) lie well in the green region proving its green emission nature in accordance with the literature studies [34]. Whereas the colour coordinates for KLAf:Dy³⁺ lie between the yellow-green region(Fig. 16b). Eu³⁺ is well known for its red-characteristic emission. Figure 16c demonstrates KLAf:Eu³⁺ colour coordinates in extreme red-region on the graph. Respective colour coordinates are also displayed on the graphs.

Likewise, CIE colour points for KNAf:Tb³⁺ (Fig. 17a) lies in yellow, KNAf:Dy³⁺ (Fig. 17b) in yellowish-green and KNAf:Eu³⁺ (Fig. 17c) in red-region of the chromaticity diagram, respectively.

**Fig. 17** CIE chromaticity coordinates(x,y) high-lighted by the star, circle and square marks on the chromaticity diagram for **a** KNAf:Tb³⁺ (1 mol%) phosphor under 355 nm excitation wavelength, **b** KNAf:Dy³⁺ (1 mol%) phosphor under 457 nm excitation wavelength, **c** KNAf:Eu³⁺ (1 mol%) phosphor under 390 nm excitation wavelength

Further, these colour coordinates (x,y) can be used to calculate other CIE chromaticity coordination parameters such as (u',v') coordinates and Correlated Colour Temperature(CCT) [46].

$$CCT = -449n^3 + 3625n^2 - 6823.3n + 5520.33 \quad (5)$$

where, $n = (x - x_e)/(y - y_e)$. (x_e, y_e) represents the coordinates of the point at the epicenter with value equal to (0.332, 0.186). CCT values are calculated in kelvin (K). Table 6 gives CCT (K) values along with (x,y) & (u',v') coordinates for KLAf:Tb³⁺, Dy³⁺, Eu³⁺ (1 mol %) phosphors. Similarly, Table 7 assembles the CCT and (x,y) & (u', v') values for KNAf:Tb³⁺, Dy³⁺, Eu³⁺ (1 mol %) phosphors. CCT(K) values greater

Table 6 CIE Chromaticity parameters for RE³⁺ doped-K₂LiAlF₆ phosphors

RE ³⁺ ion	(x,y)	(u',v')	CCT(K)	Application in w-LEDs
Tb ³⁺	0.2581,0.5407	0.1151,0.5424	7106	> 5000 K, cool
Dy ³⁺	0.3252,0.4623	0.1647,0.5269	5688	> 5000 K, cool
Eu ³⁺	0.5815,0.4176	0.3397,0.5488	1759	< 5000 K, warm

Table 7 CIE Chromaticity parameters for RE³⁺ doped-K₂NaAlF₆ phosphors

RE ³⁺ ion	(x,y)	(u',v')	CCT(K)	Application in w-LEDs
Tb ³⁺	0.4156,0.5031	0.2026,0.5518	3951	< 5000 K, warm
Dy ³⁺	0.3897,0.4616	0.2009,0.5354	4235	< 5000 K, warm
Eu ³⁺	0.5824,0.4168	0.3408,0.5487	1754	< 5000 K, warm

than 5000 K are considered good for cool white light LEDs, whereas lesser values are applicable to warm LED-lighting [47]. u' & v' coordinates can be calculated from the following formulas:

$$u' = \frac{4x}{12y - 2x + 3} \quad (6)$$

$$v' = \frac{9y}{12y - 2x + 3} \quad (7)$$

CIE colour coordinates for K₂LiAlF₆:RE³⁺ and K₂NaAlF₆:RE³⁺ along with its CCT(K) and values of u' & v' coordinates are calculated from the above formulas. Although, softwares also calculates and displays these values but it's worth to mark here that these values are found to be somewhat similar to the values that we have obtained by putting known CIE (x,y) coordinates in the above formulas separately to check the reliability of the software and our calculations. (u' , v') coordinates are useful in locating points on CIE 1976 colour chromaticity coordinate diagram.

5 Conclusion

Formation of two elpasolites K₂LiAlF₆ and K₂NaAlF₆ in pure phase was confirmed by powder-XRay Diffraction Analysis. Synthesis was successfully performed via simple Wet-chemical method. It is remarkable to observe PL emission in as-prepared powders of trivalent rare earths-activated fluoro-elpasolite hosts. Gd³⁺, Tb³⁺, Dy³⁺ and Eu³⁺, all showed their characteristic emissions in as-prepared

samples without any heat treatment. Encouraging results were observed with gadolinium activated phosphors. Sharp PL emission at 310 nm with 272 nm excitation, makes it very functional for SSL applications. Luminescence decay data curves give very long lifetime in milliseconds (ms) for these fluoride elpasolite-type structures. The minimum lifetime (τ) recorded was equal to 4.6 ms that is for 5 mol % Gd³⁺ concentration in K₂LiAlF₆, whereas 4.1 ms was observed for K₂NaAlF₆:Gd (5 mol %). Other quantities, quantum efficiency (ϕ)% and non-radiative rates (A_{nr}) have been calculated. The calculations and the experimental values indicate that with increase in dopant concentration, luminescence lifetime decreases considerably in these compounds. Decrease in lifetime takes place due to increasingly inefficient radiative energy transfers. PL was observed for other rare earth ions (Tb³⁺, Eu³⁺, Dy³⁺) also. Since emission due to Gd³⁺ lies within the UV-range, CIE colour coordinates were obtained for other three impurity ions and manifested on MacAdam ellipses. CCT(K) were computed for all the samples using Mc-Camy's equation. Further with the help of radius percentage discrepancy (D_r) equation, most probable substitution site for the rare earth ions have been investigated. It has been shown that impurity ions can easily go to K⁺ ion site in K₂LiAlF₆ but only Tb³⁺ and Eu³⁺ (among the four ions) could substitute for K⁺ in K₂NaAlF₆ host due to smaller radii size of Na⁺ ion. Transitions involved during the PL emission process in these elpasolites due to four-RE³⁺ ions have been summed up in Table 8, below:

Table 8 Summary of PL emission due to RE³⁺ ions in elpasolite phosphors (KLAF & KNAF)

RE ³⁺ ions	λ_{ex} (nm) (excitation wavelength given)	λ_{em} (nm) (emission wavelength recorded)	Transitions involved (for emission)	Combined emission in spectral range (according to CIE coordinates)
Gd ³⁺	272	305 (weak) 310 (strong)	${}^6\text{P}_{5/2} \rightarrow {}^8\text{S}_{7/2}$ ${}^6\text{P}_{7/2} \rightarrow {}^8\text{S}_{7/2}$	Ultra-violet(UV)
Tb ³⁺	285	490 (strong) 543 (very strong) 587, 590 (weak) 622 (very weak)	${}^5\text{D}_4 \rightarrow {}^7\text{F}_6$ ${}^5\text{D}_4 \rightarrow {}^7\text{F}_5$ ${}^5\text{D}_4 \rightarrow {}^7\text{F}_4$ ${}^5\text{D}_4 \rightarrow {}^7\text{F}_3$	Visible (greenish-yellow)
Dy ³⁺	350	481 (very strong) 573 (strong) 647 (very weak)	${}^4\text{F}_{9/2} \rightarrow {}^6\text{H}_{15/2}$ ${}^4\text{F}_{9/2} \rightarrow {}^6\text{H}_{13/2}$ ${}^4\text{F}_{9/2} \rightarrow {}^6\text{H}_{11/2}$	Visible (yellowish)
Eu ³⁺	390	592 (very strong) 614 (strong)	${}^5\text{D}_0 \rightarrow {}^7\text{F}_1$ ${}^5\text{D}_0 \rightarrow {}^7\text{F}_2$	Visible (orange-reddish)

Acknowledgements

This study is financially supported by CSIR, Government of India under Grant No. 31/0001(11936)/2021-EMR-I. Authors are extremely thankful to Dr. Naval Kishor Upadhyay of Advanced Carbon Products Metrology Section & Dr J. S. Tawale, CSIR—National Physical Laboratory, New Delhi for XRD, SEM and EDS measurements. Authors are also wants to show their indebt gratitude towards Ms. Sonali Mehra and Dr. Shailesh Narain Sharma of Advanced Materials & Devices Metrology Division, CSIR- National Physical Laboratory, New Delhi for DLS observations.

Author contribution

VSS: Synthesis. SRD: Writing—review & editing. PVT: Data analysis and curation. PDB: Characterization. SVM: Basic concept.

Funding

This study is financially supported by CSIR, Government of India under Grant No. 31/0001(11936)/2021-EMR-I.

Data availability

Data will be made available on reasonable request.

Declarations

Conflict of interest No potential conflict of interest was reported by the author(s).

Ethical approval This manuscript does not contain any data which needed ethical approval and the research does not involve human participants and/or animals.

References

1. I.V. Pekov, N.V. Chukanov, N.N. Kononkova, N.V. Zubkova, MKh. Rabadanov, D.Y. Pushcharovsky, Elpasolite from hyperalkaline pegmatite of the Khibiny Pluton, Kola Peninsula. Symmetry of Elpasolite. *Geol. Ore Depos.* **50**, 749–754 (2008)
2. Y.N. Zaitseva, S.D. Kirik, A.S. Samoilo, P.S. Dubinin, O.E. Bezrukova, A.N. Zaloga, S.G. Ruzhnikov, I.S. Yakimov, Solid solutions in aluminum electrolytes with the participation of LiF. *J. Sib. Fed. Univ. Chem.* **15**(1), 22–31 (2022)
3. A.S. Samoilo, Y.N. Zaitseva, P.S. Dubinin, O.E. Piksina, S.G. Ruzhnikov, I.S. Yakimov, S.D. Kirik, Structural aspects of the formation of solid solutions in the NaF-KF-AlF₃ system. *J. Solid State Chem.* **252**, 1–7 (2017)
4. K. Grjotheim, J.L. Holm, M. Malinovsky, Sh.A. Mikhaeil, The system K₃AlF₆-Li₃AlF₆ and Rb₃AlF₆-Li₃AlF₆. *Acta Chem. Scand.* **25**, 1695–1702 (1971)
5. K. Grjotheim, J.L. Holm, Sh.A. Mikhaeil, Equilibrium studies in the systems K₃AlF₆-Na₃AlF₆ and K₃AlF₆-Rb₃AlF₆. *Acta Chem. Scand.* **27**, 1299–1306 (1973)
6. G.A. Bukhalova, G.N. Maslennikova, D.M. Rabkin, Ternary system of chlorides and hexafluoroaluminates of sodium and

- potassium. *Russ. J. Inorg. Chem. (Engl. Transl.)* **7**, 847–849 (1962)
- G.A. Bukhalova, V.T. Mal'tsev, System of sodium and potassium fluorides and hexafluoroaluminates. *Russ. J. Inorg. Chem. (Engl. Transl.)* **10**, 100–102 (1965)
 - V.T. Mal'tsev, G.A. Bukhalova, Reciprocal system of fluorides, chlorides, and hexafluoroaluminates of sodium and potassium. *Russ. J. Inorg. Chem. (Engl. Transl.)* **10**, 797–800 (1965)
 - R.S. Edoyan, M.G. Manvelyan, G.G. Babayan, Physico-chemical study of the systems containing Na_3AlF_6 , K_3AlF_6 and Li_3AlF_6 . I. Melting diagram of the Na_3AlF_6 - K_3AlF_6 system. *Izv. Akad. Nauk Arm. SSR. Khim. Nauki* **18**, 10–14 (1965)
 - C.A. Sorrell, J.G. Groetsch Jr., Subsolidus compatibility in the system NaCl - KCl - AlCl_3 - NaF - KF - AlF_3 . *J. Am. Ceram. Soc.* **69**(4), 333–338 (1986)
 - P. Greenough, A.G. Pautusz, The $2\text{Eg}4\text{A}2\text{g}$ phosphorescence spectrum of the Cr^{3+} ion in K_2NaAlF_6 . *J. Chem. Phys.* **70**, 1967–1972 (1979)
 - M.A.F.M. da Silva, R.B. Barthem, L.P. Sosman, Investigation of luminescence and optical absorption of $\text{K}_2\text{LiAlF}_6:\text{Cr}^{3+}$ single crystals. *J. Solid State Chem.* **179**, 3718–3723 (2006)
 - I.N. Flerov, M.V. Gorev, K.S. Aleksandrov, A. Tressaud, J. Grannec, M. Couzi, Phase transitions in elpasolites (ordered perovskites). *Mater. Sci. Eng. R Rep* **24**, 81–151 (1998)
 - M.W. Lufaso, P.W. Barnes, P.M. Woodward, Structure prediction of ordered and disordered multiple octahedral cation perovskites using SPuDS. *Acta Cryst. B* **62**, 397–410 (2006)
 - D. Babel, R. Haegele, G. Pausewang, F. Wall, Ueber kubische und hexagonale elpasolithe $\text{A}_2\text{B}^{\text{I}}\text{M}^{\text{III}}\text{F}_6$. *Mat. Res. Bull.* **8**(12), 1371–1382 (1973)
 - V.S. Singh, C.P. Joshi, P.L. Muthal, S.M. Dhopte, S.V. Moharil, Wet chemical synthesis of Eu^{2+} activated fluoro-elpasolite phosphors. *J. Alloys Compd.* **599**, 49–52 (2014)
 - V.S. Singh, C.P. Joshi, S.V. Moharil, Wet chemical synthesis of Ce^{3+} activated fluoro-elpasolite and related fluoro-aluminate phosphors. *Opt. Mater.* **50**, 256–262 (2015)
 - S. Adachi, Review— Mn^{4+} -activated red and deep red-emitting phosphors. *ECS J. Solid State Sci. Technol.* **9**, 016001 (2020)
 - Y. Zhu, L. Huang, R. Zou, J. Zhang, J. Yu, M. Wu, J. Wanga, Q. Su, Hydrothermal synthesis, morphology and photoluminescent properties of Mn^{4+} -doped novel red fluoride phosphor elpasolite K_2LiAlF_6 . *J. Mater. Chem. C* **4**, 5690–5695 (2016)
 - X. Liu, H. Xu, Y. Zhang, Z. Fu, F. Hong, G. Pang, G. Liu, D. Li, X. Dong, J. Wang, Green synthesis, luminescent properties and application for WLED of flower-like $\text{K}_2\text{LiAlF}_6:\text{Mn}^{4+}$ phosphor. *Opt. Mater.* **119**, 111392 (2021)
 - Y. Zhu, Y. Liu, L. Huang, T. Xuan, J. Wang, Optimized photoluminescence of red phosphor $\text{K}_2\text{LiAlF}_6:\text{Mn}^{4+}$ synthesized by a cation-exchange method. *Sci. China Technol. Sci.* **60**, 1458–1464 (2017)
 - L.Y. Wang, E.H. Song, T.T. Deng, Y.Y. Zhou, Z.F. Liao, W.R. Zhao, B. Zhou, Q.Y. Zhang, Luminescence properties and warm white LED application of ternary-alkaline fluoride red phosphor $\text{K}_2\text{NaAlF}_6:\text{Mn}^{4+}$. *Dalton Trans.* **46**, 9925–9933 (2017)
 - Y. Zhu, L. Cao, M.G. Brik, X. Zhang, L. Huang, T. Xuan, J. Wang, Facile synthesis, morphology and photoluminescence of a novel red fluoride nanophosphor $\text{K}_2\text{NaAlF}_6:\text{Mn}^{4+}$. *J. Mater. Chem. C* **5**, 6420–6426 (2017)
 - T.T. Deng, E.H. Song, Y.Y. Zhou, L.Y. Wang, Q.Y. Zhang, Tailoring photoluminescence stability in double perovskite red phosphors $\text{A}_2\text{BAlF}_6:\text{Mn}^{4+}$ ($\text{A} = \text{Rb}, \text{Cs}$; $\text{B} = \text{K}, \text{Rb}$) via neighboring-cation modulation. *J. Mater. Chem. C* **5**, 12422–12429 (2017)
 - X. Yi, R. Li, H. Zhu, J. Gao, W. You, Z. Gong, W. Guo, X. Chen, $\text{K}_2\text{NaAlF}_6:\text{Mn}^{4+}$ red phosphor: room-temperature synthesis and electronic/vibronic structures. *J. Mater. Chem. C* **6**, 2069–2076 (2018)
 - H. Cheng, Y. Song, G. Liu, D. Li, X. Dong, J. Wang, W. Yu, Hydrothermal synthesis of narrow-band red emitting $\text{K}_2\text{NaAlF}_6:\text{Mn}^{4+}$ phosphor for warm-white LED applications. *RSC Adv.* **7**, 45834–45842 (2017)
 - T. Senden, R.G. Geitenbeek, A. Meijerink, Co-precipitation synthesis and optical properties of Mn^{4+} -doped hexafluoroaluminate w-LED phosphors. *Materials* **10**, 1322 (2017)
 - A.R. Kadam, R.B. Kamble, M. Joshi, A.D. Deshmukh, S.J. Dhoble, $\text{Eu}(\text{III})$, $\text{Tb}(\text{III})$ activated/co-activated K_2NaAlF_6 host array: simultaneous approach for improving photovoltaic efficiency and tricolour emission. *New J. Chem.* **46**, 334–344 (2022)
 - I. Gupta, S. Singh, S. Bhagwan, D. Singh, Rare earth (RE) doped phosphors and their emerging applications: a review. *Ceram. Int.* **47**, 19282–19303 (2021)
 - E.J. Bosze, G.A. Hirata, L.E. Shea-Rohwer, J. McKittrick, Improving the efficiency of a blue-emitting phosphor by an energy transfer from Gd^{3+} to Ce^{3+} . *J. Lumin.* **104**, 47–54 (2003)
 - Y. Shi, G. Ge, L. Yang, C. Li, Z. Wang, Structure and photoluminescence properties of $\text{Ca}_2\text{GdZr}_2\text{Al}_3\text{O}_{12}:\text{RE}^{3+}$ ($\text{RE}^{3+} = \text{Eu}, \text{Sm}, \text{Pr}, \text{Dy}, \text{Tb}$) phosphors. *J. Mater. Sci. Mater. Electron.* **29**, 771–777 (2018)
 - K. Binnemans, C. Gorller-Walrand, J.L. Adam, Spectroscopic properties of Gd^{3+} -doped fluorozirconate glass. *Chem. Phys. Lett.* **280**, 333–338 (1997)
 - P. Sehrawat, A. Khatkar, S. Devi, A. Hooda, S. Singh, R.K. Malik, S.P. Khatkar, V.B. Taxak, An effective emission of

- characteristic cool white light from Dy^{3+} doped perovskite type $\text{SrLa}_2\text{Al}_2\text{O}_7$ nanophosphors in single-phase pc WLEDs. *Chem. Phys. Lett.* **737**, 136842 (2019)
34. J. Dalal, A. Khatkar, M. Dalal, V.B. Taxak, S.P. Khatkar, Characteristics of down conversion green emitting $\text{Ba}_3\text{Bi}_2(\text{PO}_4)_4:\text{Tb}^{3+}$ nanosized particles for advanced illuminating devices. *J. Mater. Sci. Mater. Electron.* **31**, 1216–1226 (2020)
35. P. Phogat, V.B. Taxak, R.K. Malik, Crystallographic and optical characteristics of ultraviolet-stimulated Dy^{3+} -doped $\text{Ba}_2\text{GdV}_3\text{O}_{11}$ nanorods. *J. Electron. Mater.* **51**, 4541–4554 (2022)
36. K.S. Thomas, S. Singh, G.H. Dieke, Energy levels of Tb^{3+} in LaCl_3 and other chlorides. *J. Chem. Phys.* **38**, 2180–2190 (1963)
37. J. Liao, B. Qiu, H. Wen, W. You, Y. Xiao, Synthesis and optimum luminescence of monodispersed spheres for BaWO_4 -based green phosphors with doping of Tb^{3+} . *J. Lumin.* **130**, 762–766 (2010)
38. T.W. Kuo, T.M. Chen, Synthesis and luminescence properties of Eu^{3+} , Ce^{3+} and Tb^{3+} -activated $\text{Sr}_3\text{La}_2(\text{BO}_3)_4$ under UV excitation. *J. Lumin.* **130**, 483–487 (2010)
39. P.B. Deshmukh, S.P. Puppalwar, N.S. Dhoble, S.J. Dhoble, Optical properties of $\text{CaAl}(\text{SO}_4)_2\text{Br}:\text{RE}$ (RE = Dy, Eu, Ce) novel phosphors. *Luminescence* **29**, 609–613 (2014)
40. Y. Deng, S. Yi, Y. Wang, J. Xian, Synthesis and photoluminescence characteristics of Ln^{3+} (Ln = Sm, Er and Dy)-doped $\text{BaGd}_2(\text{MoO}_4)_4$ phosphors. *Opt. Mater.* **36**, 1378–1383 (2014)
41. B. Grobelna, A. Synak, P. Bojarski, K. Szczodrowski, B. Kuklinski, S. Raut, K. Szczodrowski, I. Gryczynski, Synthesis and luminescence characteristics of Dy^{3+} ions in silica xerogels doped with $\text{Ln}_{2-x}\text{Dy}_x(\text{WO}_4)_3$. *Opt. Mater.* **35**, 456–461 (2013)
42. A. George, S. Gopi, E. Sreeja, T. Krishnapriya, A.C. Saritha, C. Joseph, N.V. Unnikrishnan, P.R. Biju, Host sensitized tunable luminescence of single phase white light emitting $\text{Ca}_2\text{Sb}_2\text{O}_7:\text{Eu}^{3+}$ phosphors. *J. Mater. Sci.: Mater. Electron.* **31**, 423–434 (2020)
43. J. Dalal, M. Dalal, S. Devi, R. Devi, A. Hooda, A. Khatkar, V.B. Taxak, S.P. Khatkar, Structural analysis and Judd-Ofelt parameterization of $\text{Ca}_9\text{Gd}(\text{PO}_4)_7:\text{Eu}^{3+}$ nanophosphor for solid-state illumination. *J. Lumin.* **210**, 293–302 (2019)
44. M.Z. Farah Khaleda, B. Vengadaesvaran, N.A. Rahim, Chapter 18—Spectral response and quantum efficiency evaluation of solar cells: a review, in *Energy materials-fundamentals to applications*. (Elsevier, 2021), pp.525–566
45. P. Cai, L. Qin, C. Chen, J. Wang, S. Bi, S.I. Kim, Y. Huang, H.J. Seo, Optical thermometry based on vibration sidebands in $\text{Y}_2\text{MgTiO}_6:\text{Mn}^{4+}$ double perovskite. *Inorg. Chem.* **57**, 3073–3081 (2018)
46. C.S. McCamy, Correlated color temperature as an explicit function of chromaticity coordinates. *Color Res. Appl.* **17**, 142–144 (1992)
47. J. Xiang, M. Yang, Y. Che, J. Zhu, Y. Mao, K. Xiong, H. Zhao, Photoluminescence investigation of novel reddish-orange phosphor $\text{Li}_2\text{NaBP}_2\text{O}_8:\text{Sm}^{3+}$ with high CP and low CCT. *Ceram. Int.* **45**, 7018–7024 (2019)

Publisher's Note Springer Nature remains neutral with regard to jurisdictional claims in published maps and institutional affiliations.

Springer Nature or its licensor (e.g. a society or other partner) holds exclusive rights to this article under a publishing agreement with the author(s) or other rightsholder(s); author self-archiving of the accepted manuscript version of this article is solely governed by the terms of such publishing agreement and applicable law.